Ionic liquids/metal reactivity: on the origins of cation–anion synergy to form stable grafted molecules

Christophe Méthivier, Mireille Turmine, Vincent Vivier, Oumaïma Gharbi

Applied Surface Science 732 (2026) 166518

Contents lists available at ScienceDirect

Applied Surface Science

journal homepage: www.elsevier.com/locate/apsusc

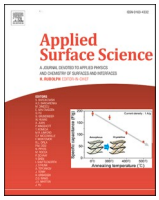

Full Length Article

Ionic liquids/metal reactivity: on the origins of cation–anion synergy to form stable grafted molecules

Christophe Méthivier, Mireille Turmine, Vincent Vivier, Oumaïma Gharbi *

Sorbonne Université, CNRS, Laboratoire de Réactivité de Surface, 4 Place Jussieu, F-75005 Paris, France

ARTICLE INFO

Keywords:
In situ XPS
In situ PM-IRRAS
Ethylammonium nitrate
Nitrate reduction

ABSTRACT

In this work, the reactivity between a Cu single crystal (110) and an alkylammonium ionic liquid – the ethylammonium nitrate (EAN) – was investigated by in situ X-ray photoelectron spectroscopy (XPS) and polarization modulation infrared reflectance absorbance spectroscopy (PM-IRRAS). EAN molecules were successfully deposited in the UHV XPS chamber at different surface coverages and the results revealed the strong nitrate anion and ammonium cation reactivity towards the Cu (110) single crystal. In addition, important variations in the anion reactivity towards the Cu single crystal was shown when the cation nature was changed (comparison of EAN, sodium nitrate and ammonium nitrate). In fact, PM-IRRAS results revealed that such variations in reactivity arise from different nitrate orientation towards the substrate, confirming, at the molecular level, the presence of the so-called cation–anion synergy. These findings provide fundamental prospects enabling more thought-through designs of task specific and environmentally friendly ionic liquids for broader applications, including electrocatalysis and heterogeneous catalysis.

1. Introduction

Ionic liquids are increasingly used as alternative solvents in electrochemical materials science, for applications ranging from electrocatalysis, energy applications, or corrosion science and corrosion protection [1–3]. The main reason behind such enthusiasm is their attractive physicochemical and electrochemical properties. Indeed, ionic liquids are defined as salts with a melting temperature below 100°C, and are characterised by a high chemical and thermal stability together with a negligible vapour pressure [1]. In addition, the quasi-infinite possibilities in terms of cation–anion combinations open the path to the design of novel, task specific and environmentally friendly solvents.

For instance, in the context of corrosion protection, ionic liquids have been explored over the past decades as next-generation coatings or potential corrosion inhibitors for the replacement of chromate-based coating formulations [2,4,5]. In fact, several ionic liquid families have been explored, for carbon steel, mild steel, and even magnesium alloys [6], and were either used as corrosion inhibitors or as conversion coatings [7–10]. The rationale behind it is to explore possible synergistic effects between the cation and the anion, in order to develop enhanced and task-specific corrosion inhibitors. For example, synergistic effects in corrosion inhibition have been previously reported for cinnamate-based rare earth corrosion inhibitors [11,12]. The authors reported a significant increase of the inhibition properties of rare earth compounds with the addition of the carboxylate anion. They observed the formation of metal-cinnamate complexes via Attenuated Total Reflectance Fourier Transform Infrared spectroscopy (ATR-FTIR) as well as the formation of rare earth metal hydroxides as the initial steps of the protective film formation [11,12]. More recently, Chong et al. also reported the presence of a synergistic corrosion inhibition process for imidazolinium-based ionic liquids used on mild steel [3]. In this context, it is clear that most of the research work seems to agree on the principle of synergistic effect between the cation and the anion [3,13]. However, the molecular scale mechanism underlying such synergy remains unclear. Recent work from Benbouzid et al. described the inhibition mechanism of an alkylammonium ionic liquid family (ethylammonium, propylammonium and butylammonium nitrate) on the corrosion of an Al-Cu-Mg alloy (AA2024-T6) [5]. In this study, the authors reported the presence of the so-called cation–anion synergy in the inhibition process of the AA2024-T6. Electrochemical results revealed that the ionic liquid impacted the anodic kinetics, by promoting alloy passivation, which was attributed to the presence of the nitrate anions (NO_3^-). Unexpectedly, the presence of the ammonium cation was shown to further decrease the

* Corresponding author.
E-mail address: oumaima.gharbi@sorbonne-universite.fr (O. Gharbi).

https://doi.org/10.1016/j.apsusc.2026.166518
Received 28 September 2025; Received in revised form 15 January 2026; Accepted 3 March 2026
Available online 6 March 2026

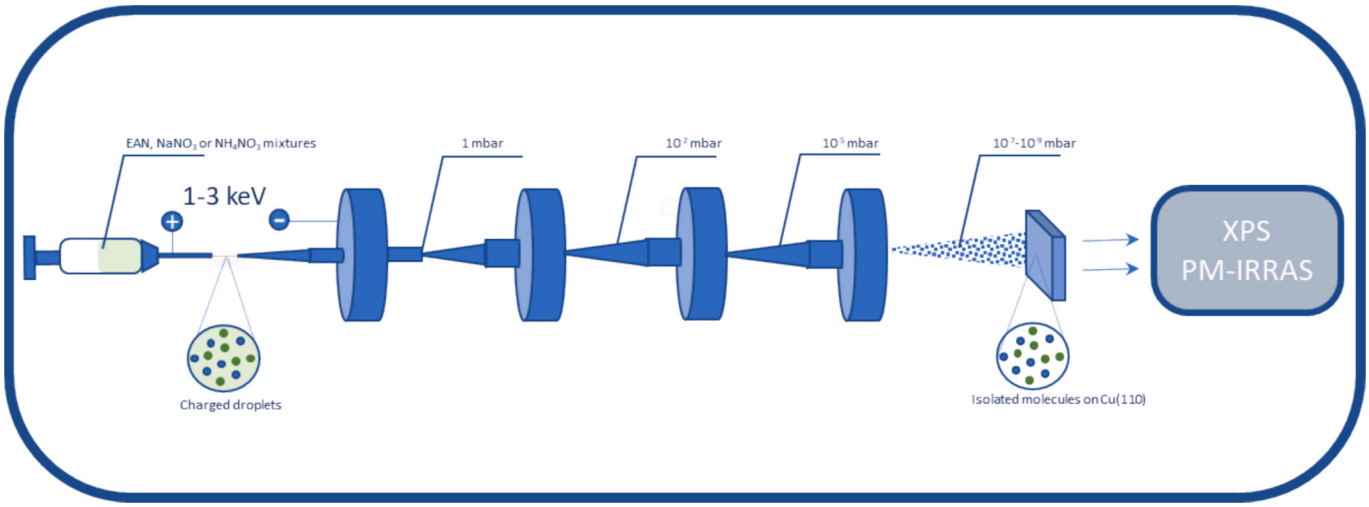

Fig. 1. General principle of the electrospray ionisation technique used in the context of this work and consisting of a syringe filled with the mixture of the element of interest and a solvent (isopropanol in this case). The syringe is used to introduce the solution progressively and an electric field is applied to produce charged droplets that will be transported gradually to the ultra-high vacuum PM-IRRAS chamber.

anodic kinetics by an order of magnitude. In addition, the length of the cation alkyl chain seemed to have a negligible impact on the anodic kinetics, suggesting that the ammonium head was primarily involved in this anion-cation synergy. Conversely, the cathodic kinetics, which was assigned to the oxygen and nitrate reduction reactions, was not impacted by the presence of the cation. However, the alkyl chain length seemed to play a role in the reduction kinetics by acting like a barrier at the interface to chloride ion penetration. The results clearly suggested the presence of a cation–anion synergy without providing a clear explanation its origins. In addition, several aspects of the inhibition mechanisms remain unclear. The first uncertainty is related to the role of the ethylammonium cation on the reaction mechanism, and how its presence increases significantly the inhibition properties (i.e reactivity) of the nitrate anion. The second unknown is how the ionic liquids interact with the cathodic sites, which are in this alloy, mostly Cu-rich intermetallic particles.

The objective of this work is to further investigate the reactivity of the ethylammonium nitrate ionic liquid and to decipher the origins of the synergism by using a surface science approach. Herein, to model the reactivity of Cu-rich intermetallic particles, which are found in Al-Cu-Mg alloys and previously shown to also have a high reactivity towards the ionic liquid (by their selective dissolution), a Cu (110) single crystal is used. The ionic liquid is introduced into the PM-IRRAS chamber via electrospray ionisation, allowing the deposition of ethylammonium nitrate molecules on the substrate at different coverages, ranging from sub-monolayer to several layers. The interface molecule/copper single crystal will be monitored in situ via X-ray photoelectron spectroscopy (XPS) and polarisation modulation infrared reflectance absorbance spectroscopy (PM-IRRAS) (see Fig. 1). The coupling of these two techniques will provide information on the surface and the ionic liquid reactivity in term of interfacial bonding, ordering and molecule orientation towards the surface. The real time analysis of the system will provide, at the molecular level, an in-depth understanding of the origins of the cation/anion synergy. Beyond corrosion, such an approach also opens promising perspectives in the field of catalysis, as surface science enables a molecular-level understanding of reaction mechanisms.

2. Experimental

2.1. Ionic liquids synthesis & solutions

The ethylammonium nitrate (EAN) ionic liquid was synthesised via an acid-base reaction consisting of adding concentrated nitric acid (67% in water from VWR) dropwise to an ethylamine solution (70% in water from thermoscientific) under vigorous mixing and in a temperature-controlled cell (kept at −5°C) at a 1:1 M ratio. The ionic liquid is subsequently freeze-dried several times at −86°C and 38 mTorr to decrease its water content (below 100 ppm), as measured by a Karl Fisher coulometric titrator. Sodium nitrate ($NaNO_3$) and ammonium nitrate (NH_4NO_3) salts were purchased from sigma Aldrich (>99.0%). The reagents were dissolved in a polar solvent, volatile enough to allow their introduction into the vacuum using the electrospray deposition technique (vide infra). Ethylammonium nitrate (1 mM) was mixed with pure isopropanol >99.7% from VWR, and water/ethanol mixtures (1/4 in volume) were used for $NaNO_3$ (1 mM) and NH_4NO_3 (1 mM). Two different solvents (isopropanol and ethanol) were employed to optimise the solubility/miscibility of the molecules. The possible presence of solvent in the UHV chamber was assessed via XPS measurement after electrospray at 110 K. No solvent-related XPS signal was detected after physisorption, as evidenced by the molar concentration ratios calculated from the XPS O 1s peak. These ratios indicate that only the target molecules were physisorbed at 110 K, with no detectable contribution from the solvents (Table 1).

Table 1
Molar concentration ratios with respect to oxygen (a) computed using theoretical stoichiometry of the molecules, (b) determined from XPS peaks for molecules adsorbed at 110 K, (c) determined from XPS peaks after going back to room temperature.

		N 1s	C 1s	Na 1s
$NaNO_3$	(a)	0.333	–	0.333
	(b)	0.326	–	0.294
	(c)	0.347	–	0.384
NH_4NO_3	(a)	0.666	–	–
	(b)	0.649	–	–
	(c)	0.397	–	–
EAN	(a)	0.666	0.666	–
	(b)	0.633	0.645	–
	(c)	0.463	0.5	–

2.2. Electrospray technique

The electrospray deposition in vacuum chamber is a common route

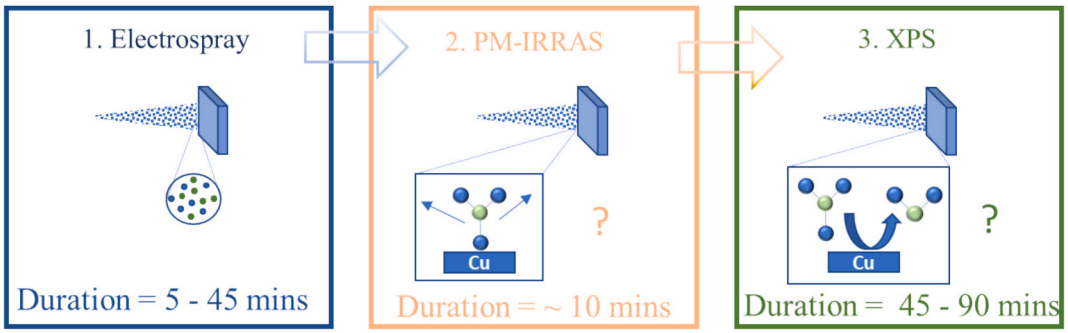

Fig. 2. Schematic illustration of the experimental protocol used in this work, consisting of the electrospray, followed by PM-IRRAS analysis, and finally the XPS acquisition.

for the deposition of non-volatile molecules such as salts and is, therefore, well suited for the deposition of ionic liquids molecules. Herein, a system from Molecular Spray ltd. (UK) was used. The general principle consists of introducing the molecular solution in a syringe at room temperature. A voltage of 2 kV is applied to a flow rate of 10 µL/min to the syringe needle producing charged droplets of liquids at its tip. These droplets enter the first vacuum chamber through a 250 µm-diameter capillary. Three differential pumping stages allow the evaporation of the solvent, followed by the fission of the droplets, ultimately producing isolated molecules arriving on the surface. During the electrospray deposition, the pressure in the main chamber was in the 10^{-7}–10^{-9} mbar (or 10^{-7} Torr range).

2.3. Surface characterisation

The reactivity of the ethylammonium nitrate with the Cu single crystal was monitored in real time using X-ray photoelectron spectroscopy (XPS), coupled with polarisation-modulation infrared reflection absorption spectroscopy (PM-IRRAS) in ultra-high vacuum (UHV) adjacent chambers.

XPS measurements were performed after each electrospray deposition step using a SPECS (Phoibos 100-1D-DLD) spectrometer equipped

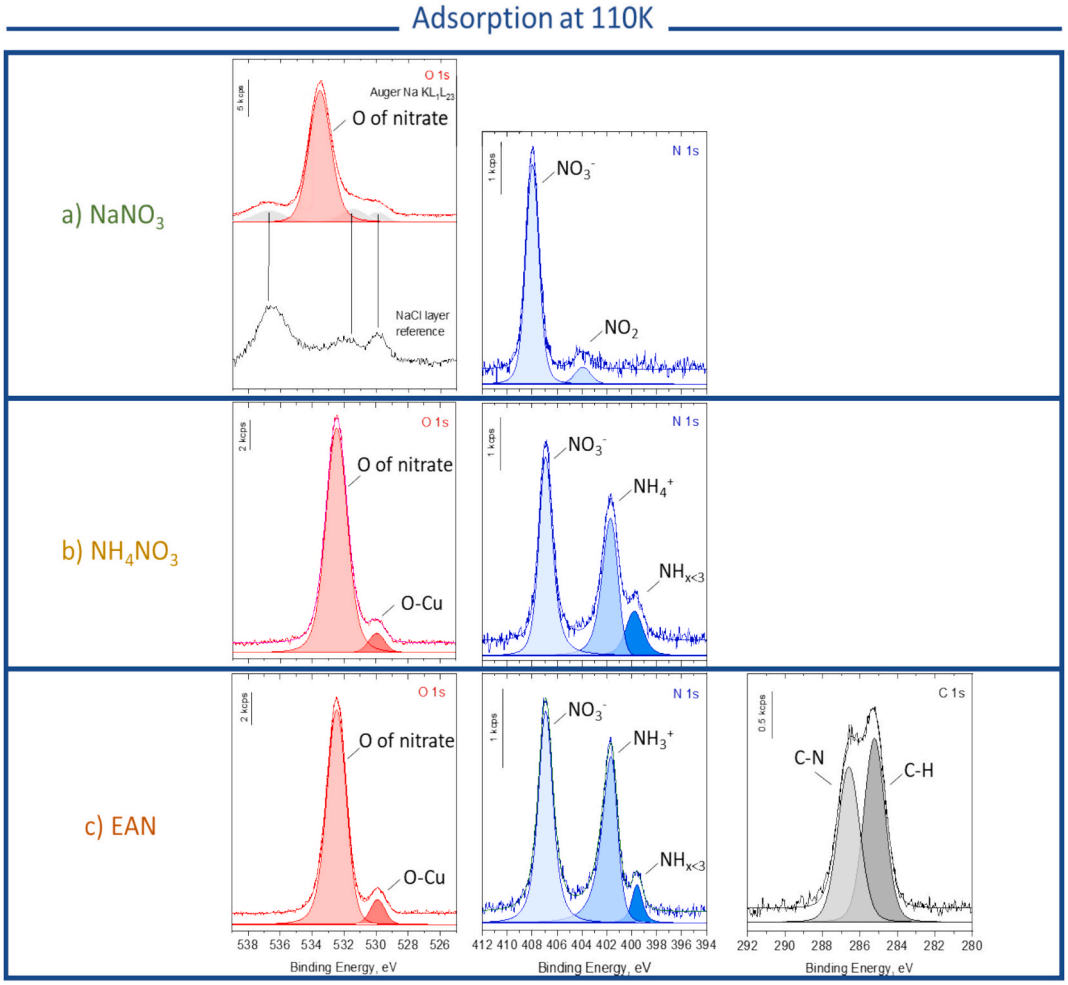

Fig. 3. XPS spectra of O1s, N1s and C1s recorded for a) $NaNO_3$, b) NH_4NO_3 and c) EAN after adsorption on the Cu (110) single crystal at 110 K, revealing the successful adsorption of each molecule on the surface.

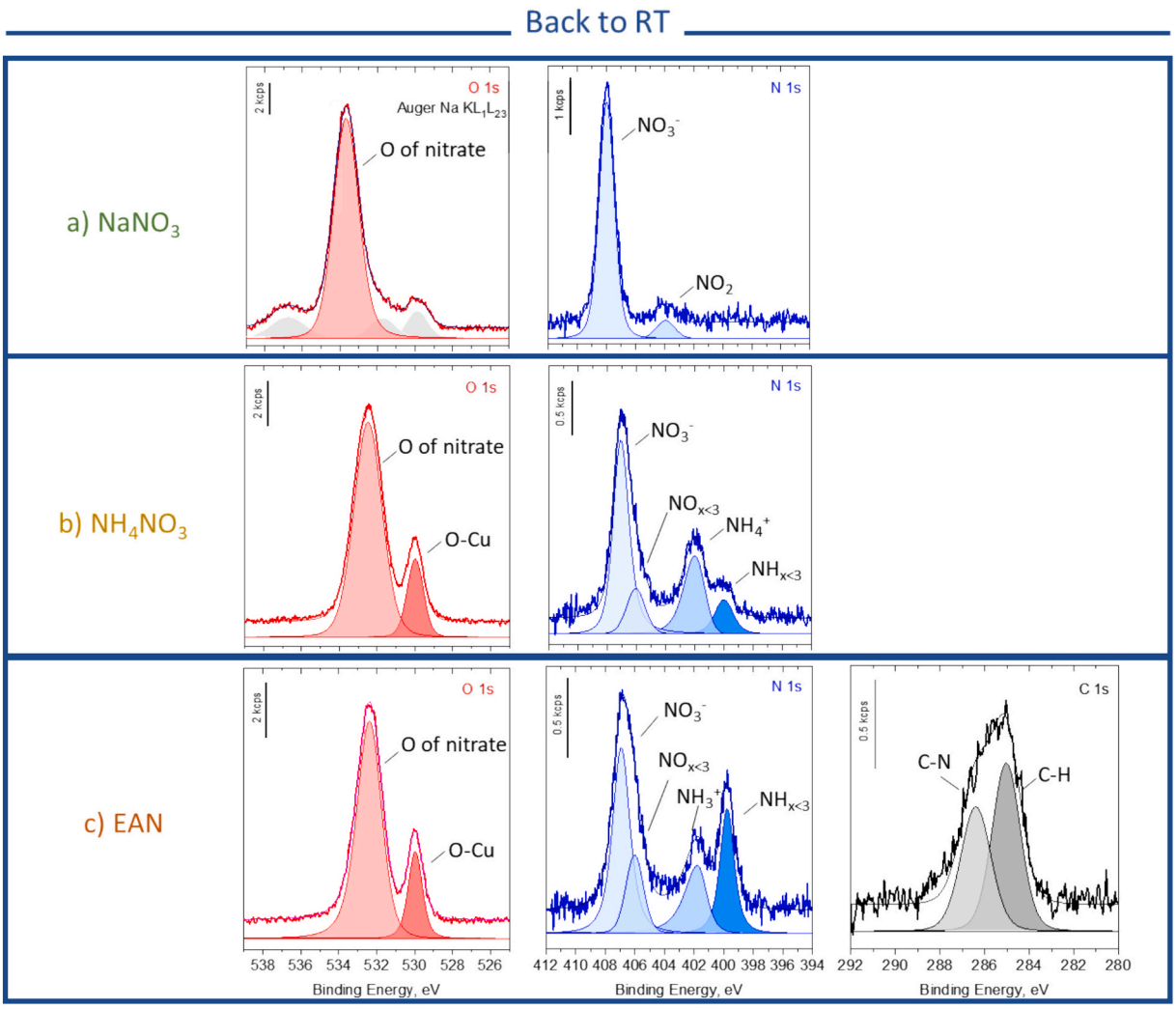

Fig. 4. XPS spectra of O1s, N1s and C1s peaks recorded for a) $NaNO_3$, b) NH_4NO_3 and c) EAN after leaving the system going back to RT. The results reveal the existence of an oxygen peak associated with the Cu (110) single crystal oxidation at 530 eV, concomitant with the change in the intensities of the peaks in the N1s spectra associated with the ammonium cation, and the deprotonated ammonium species as well as the intensity ratios of the [C–N] and [C–H] of the C 1s spectra for the EAN.

with a monochromatised Al Kα X-ray source (hv = 1486.6 eV) operated at 16 mA and 14 kV. The Cu (110) single crystal was fixed on a support, and no charge compensation device was used on the sample. Herein, the photoelectron collection angle, θ, corresponding to the angle between the normal to the sample surface and the analyser axis was equal to 0°. A survey spectrum was systematically acquired at 100 eV pass energy, followed by high-resolution spectra of Cu 2p, C 1s, N 1s, O 1s, Cu 3p, Auger Cu $L_3M_{45}M_{45}$, and Auger $NaKL_1L_{23}$ peaks acquired with a 20 eV pass energy. Under high-resolution narrow scan conditions, the full width at half maximum (FWHM) of the Ag $3d_{5/2}$ peak of a standard clean silver sample was 0.6 eV. The spectrometer was calibrated by setting the Fermi level to zero on the binding energy scale. Without additional referencing procedure, the calibration led to a binding energy position of the Cu $2p_{3/2}$ peak found at 932.6 ± 0.1 eV. Data analysis was performed using the Casa XPS software (Casa Software ltd., UK). The peaks were decomposed using a U2 Tougaard baseline and a component shape defined by a convolution product of a Lorentzian and a Gaussian function (Casa XPS LA(x,y) lineshape where x controls the tail spread of the Lorentzian part and y controls the width of the Gaussian part) [14] (see supplementary information for the decomposition parameters).

A Nicolet 5700 FT-IR spectrometer was used to acquire the PM-IRRAS spectra. Prior to the reflection of the IR beam on the sample, a ZnSe grid polariser and a photoelastic modulator were placed in the beam path to modulate the incident beam between p- and s-polarisation. After specular reflection of the incident beam at an angle of 85° with respect to the normal to the surface, the IR light was focused onto a nitrogen-cooled MCT wide-band detector. The UHV chamber and the spectrometer were interfaced through the ZnSe windows. In this work, each spectrum was acquired from 1024 scans at a resolution of 8 cm^{-1}. Before the molecule adsorption, the Cu (110) single crystal was cleaned under vacuum using 1 keV Ar^+ ion sputtering, followed by annealing at 850 K to ensure the absence of residual contamination. All experiments were reproduced between 2 and 5 times to ensure reproducibility.

The experimental procedure consisted of two different approaches, as shown in Fig. 2. The first one consisted of performing the electrospray deposition of the EAN mixture on the Cu (110) at 110 K in order to obtain reference XPS and PM-IRRAS spectra for the molecule. The electrospray procedure was followed by PM-IRRAS measurements with an acquisition time of around 10 mins and then by an XPS acquisition of ~45 mins. After acquisition, the system was allowed to return to room temperature (RT) and the reactivity of the deposited layer was monitored *via* PM-IRRAS and XPS analysis. A second approach consisted in performing several electrospray depositions at room temperature, in order to monitor the kinetics of the ethylammonium nitrate reactivity towards the substrate. To dissociate the effect of the anion and the cation, two other salts were used in this study, namely sodium nitrate

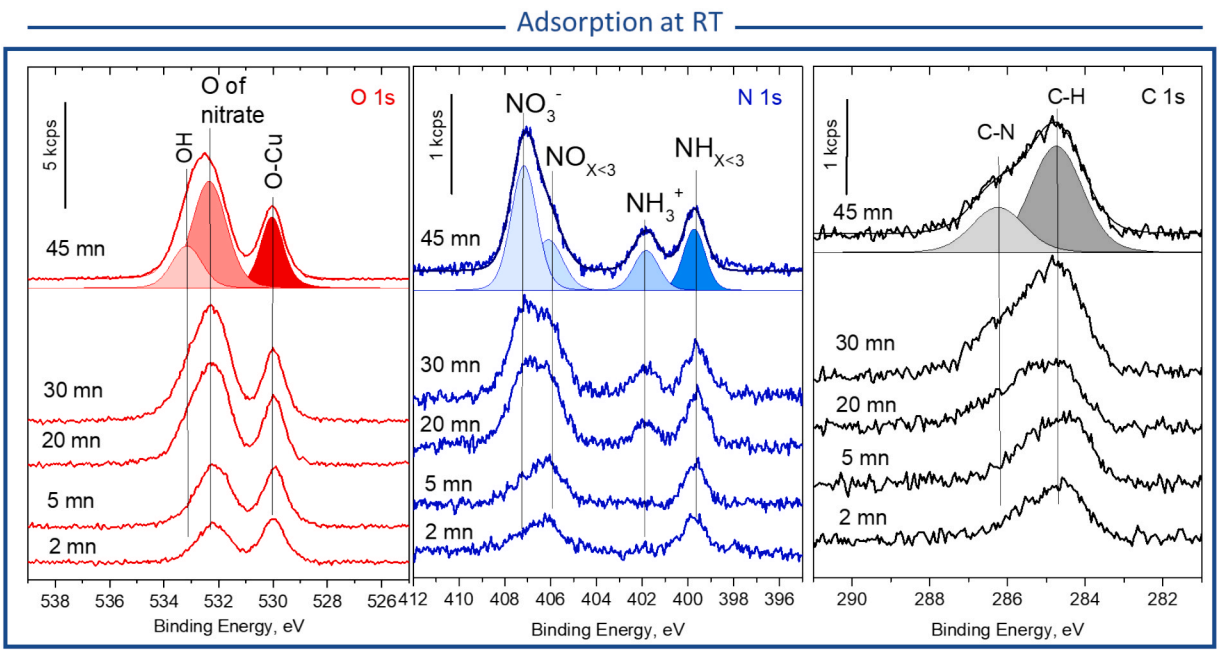

Fig. 5. XPS spectra of O1s, N1s and C1s peaks recorded after the adsorption of EAN at RT on the Cu single crystal after increasing electrospray time.

($NaNO_3$) and ammonium nitrate (NH_4NO_3) and similar experimental procedures were carried out for both systems.

3. Results

3.1. a) Adsorption at 110 K

The adsorption of $NaNO_3$, NH_4NO_3 and EAN mixtures were initially performed at 110 K (which corresponds to the lowest temperature achievable by our experimental set-up) to ensure that the molecules were successfully physisorbed on the Cu (110) single crystal in their pristine state following the electrospray deposition step, thereby enabling real time monitoring of the molecule reactivity (Fig. 3). These two conditions were deliberately selected to represent extreme scenarios: one characterised by minimal reactivity with the substrate and another in which significant surface oxidation is observed. The XPS spectra measured after the physisorption step of $NaNO_3$, NH_4NO_3 and EAN are presented in Fig. 3a, b and c respectively. Herein, O1s, N1s, C1s and $NaKL_2L_{23}$ secondary Auger peaks were recorded for each molecule. For $NaNO_3$, the O1s spectrum exhibit a main peak at 533.5 eV corresponding to the oxygen–nitrogen bond, and a second peak at 537 eV which is attributed to the secondary Na Auger peaks, $NaKL_1L_{23}$. Two additional contributions at 529 eV and 531 eV are related to the complex structure of the Na Auger signal, as confirmed by a reference spectrum on pure NaCl recorded in the absence of oxygen on the surface (labelled as NaCl reference on Fig. 3). The N1s single peak at 408 eV is associated to the nitrogen atom linked to the oxygen, clearly indicating that the nitrate anion was successfully physisorbed on the Cu substrate, and a second small contribution observed at 404 eV, which may indicate the partial dissociation of the NO_3^- to NO_2^-, most likely due to a reaction with the substrate. Similarly, the O1s of the NH_4NO_3 displays a major peak at 532.5 eV associated with the oxygen atoms bound with the nitrogen [**O**-N], and a second smaller component at 530 eV, usually attributed to oxygen bound to Cu metal [**O**-Cu], revealing a partial oxidation of the Cu (110) single crystal after the NH_4NO_3 adsorption. The N1s XPS spectrum can be deconvoluted into three components which are attributed to the nitrogen atom bound to the oxygen present in the NO_3^- anion, [**N**-O] found at 406.9 eV, a second at 401.8 eV corresponding to the nitrogen present in the ammonium cation [$\underline{N}H_4^+$], and a last component which is ascribed to the partial deprotonation of ammonium cations yielding to the presence of a peak at 399.8 eV. As for $NaNO_3$ and NH_4NO_3, the EAN XPS results of the O1s peak reveal a main component at 532.4 eV associated with oxygen bonded to nitrogen [**O**-N] and an additional weak component at 530 eV, corresponding to oxygen [**O**-Cu] bound to Cu surface, probably caused by a partial oxidation induced by the EAN molecule on the substrate. A slight shift in the N1s binding energy is observed among $NaNO_3$, NH_4NO_3, and EAN, likely due to subtle variations in their chemical environments. The N1s peak displays three components: one at 406.9 eV attributed to the nitrogen of the nitrate [**N**-O]; one at 401.7 eV associated with the nitrogen comprised in the ammonium cation [**N**–H] (from $C_2H_5NH_3^+$); and one at 399.8 eV corresponding to the partial deprotonation of the molecule, due to possible interaction of the molecule with the substrate, despite keeping the system at 110 K. The carbon peak is composed of one doublet with a 1:1 intensity ratio attributed to the carbon atoms of the ammonium cation alkyl chain [**C**–N] at 286.4 eV and [**C**–H] at 285 eV [15,16]. The results clearly indicate that the molecules are predominantly remain largely intact after deposition at 110 K, as further supported by the molar concentration ratios reported in Table 1.

3.2. b) Reactivity of EAN, $NaNO_3$ and NH_4NO_3 at RT

After the adsorption of the molecules at 110 K, the system was returned to room temperature (RT), and XPS measurements were conducted after equilibration (Fig. 4). The results differ significantly from those obtained at 110 K, particularly for the ammonium nitrate and ethylammonium nitrate, suggesting a substantial reactivity with the Cu (110) surface. Indeed, a significant Cu oxidation at RT is shown by the 530 eV O1s, revealing a reaction between the molecules and the substrate, as in these conditions, Cu alone should not experience oxidation at RT in the UHV chamber. Interestingly, for $NaNO_3$, only minor changes are observed in the O1s region, with one main component at 533.5 eV, two minor components at 537 eV and 529 eV, which were attributed previously to the $NaKL_1L_{23}$ Auger peak. The N 1s peak for $NaNO_3$ consists of one main peak at 408 eV attributed to the nitrogen bound to the oxygen in the nitrate anion [**N**-O], and a weak contribution at 404 eV attributed to NO_2^- species. The slight reduction of NO_3^- to NO_2^- species

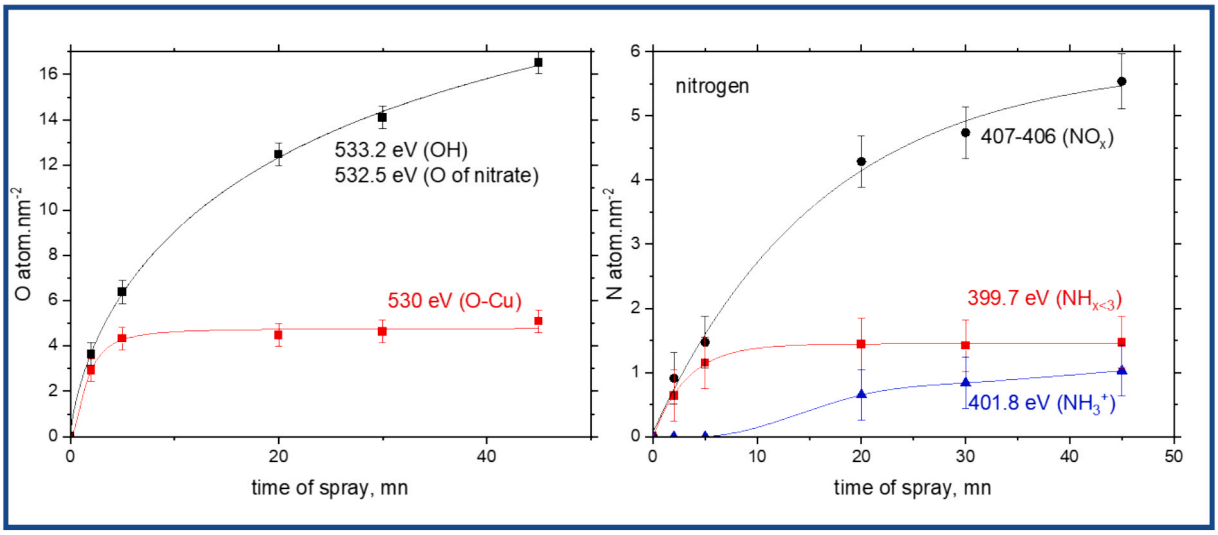

Fig. 6. a) Number of oxygen atoms and b) nitrogen atoms per nm^2 as a function of spray time. Two different binding energies were monitored for both oxygen and nitrogen, revealing that the 530 eV 1s O and 400 eV 1s N binding energies are related to species located at the interface, which completely covered the Cu (110) surface afte ~5 mins of spray time.

suggests a low reactivity of the nitrate anion towards the Cu (110) single crystal under these conditions. In contrast, major changes are observed for NH_4NO_3 and EAN. In both cases, the intensity of the O1s component at 530 eV increases significantly (in addition to the 532.4 eV peak from [**O**-N] in NO_3^-), confirming copper oxidation and formation of [**O**-Cu] species. In addition, the N1s spectra show a strong peak at 407 eV, which can be deconvoluted to include a second contribution at 406 eV associated to NO_3^- species and resulting nitro-compounds ($NO_{x<3}$) respectively. These species appear only after thermal relaxation to RT, suggesting the formation of secondary nitro-based species via NO_3^- reduction on Cu (110). These findings are in good agreement with the observations made on the O 1s XPS spectra of NH_4NO_3 and EAN, for which a peak at 530 eV corresponding to Cu oxidation [**O**-Cu] was observed. Fig. 4 illustrates the evolution of the O 1s, N 1s, and C 1s peaks for all three systems.

Additional insights are provided by the N1s spectra. Peaks at 402 eV and 400 eV are ascribed to protonated amines [C-**N**H_3^+] and deprotonation ammonium species [C-**N**$H_{x<3}$], respectively, suggesting a surface reaction between the copper substrate and the ammonium cation. In addition, the peak at 399.8 eV in the N1s spectra becomes more intense for EAN than for NH_4NO_3 and compared to the spectra acquired at 110 K, indicating the possible formation of a [Cu–**N**] bond between copper and the ammonium nitrogen. Simultaneously, the C1s peaks (286.4 eV and 285 eV) associated with [C-NH_3^+] and [**C**–H], undergo noticeable changes. A significant decrease in the [**C**–N] suggests partial cleavage of the ammonium alkyl chain. These observations are consistent with the evolution of the N1s peaks of the EAN, which show low binding energy features attributed to the deprotonation or the formation of [Cu–**N**] at the interface. These observations are further supported by the concentration ratios determined from the results and shown in Table 1, revealing a significant loss of nitrogen, with the O/N ratio increasing from 1.5 to 2.4 for NH_4NO_3 and to 2.2 for EAN.

3.3. c) Reactivity and layer thickness evolution of EAN at room temperature as a function of electrospray time

The reactivity of the EAN molecules was subsequently monitored over 45 mins of electrospray at RT (Fig. 5). The O1s spectra confirm the trend previously observed, with the presence of the [O-Cu] contribution at 530 eV, as early as 2 min of the electrospray, suggesting a high reactivity (i.e., rapid oxidation) of the Cu substrate towards the EAN. Interestingly, the 532.4 eV contribution corresponding to the [**O**-N] of the NO_3^- continues to increase and a shoulder at higher binding energy (533 eV) appears after 5 min, possibly the formation of surface hydroxyls, most likely due to ammonium, a point discussed in more details later. This evolution could reflect a change in the chemical environment of the NO_3^- species, which could be due to both interfacial NO_3^- and bulk NO_3^- (i.e., not in direct contact with the Cu surface). The N1s spectra reveal important variations as a function of the electrospray time. In the first 5 min, only two weak contributions are observed, corresponding to [**N**-$O_{x<3}$] at 406 eV and [**N**-$H_{x<3}$] at 400 eV, respectively. These features suggest that the EAN molecules electrosprayed during the first 5 min directly interact with the Cu surface and undergo rapid decomposition, forming nitro – nitrito compounds. It is only after 20 mins of electrospray that significant changes appear, with first a broadening and increase in intensity of the initial [**N**-$O_{x<3}$] contribution at 407 eV, while a new contribution emerges at 402 eV. These two components are attributed to the presence of NO_3^- species, as previously reported for the spectra at 110 K, and to the protonated amine contribution [C-**N**H_3^+], which indicates the presence of multilayers of EAN deposited on the substrate. In addition, the C1s spectra corroborate this interpretation, with the presence of an initial peak at 285 eV associated with the [**C**–H] bond.

A second key objective was to determine whether the ionic liquid forms multilayers on the surface. To address this, the evolution oxygen and nitrogen surface density (atoms per nm^2) was monitored at different electrospray durations at room temperature, as illustrated in Fig. 5, using two and three binding energies, respectively. The layer thickness (d, in nm), was calculated from the XPS data using Eq. (1), assuming a uniform film on a semi-infinite substrate:

$$n_{layer}.d = \frac{I_{layer}\rho_{Cu}\sigma_{Cu}T_{AugerCu}\lambda^{Cu}_{AugerCu}}{I_{AugerCu}M_{Cu}\sigma_{layer}T_{layer}} \quad (1)$$

where n_{layer} is the number of atoms per volume unit (thus, $n_{layer}.d$ is the number of atoms per surface unit), $I_{AugerCu}$ and I_{layer} are the intensities of the selected peaks (Auger Cu $L_3M_{45}M_{45}$ and O1s and N1s at two binding energies, respectively in Fig. 3a and b). T_{layer} and $T_{AugerCu}$ are the transmission values provided by the spectrometer manufacturer at the kinetic energy of the O1s (layer), N1s (layer) and Auger Cu $L_3M_{45}M_{45}$, respectively. σ is the Scofield photoionisation cross sections for O1s, N1s

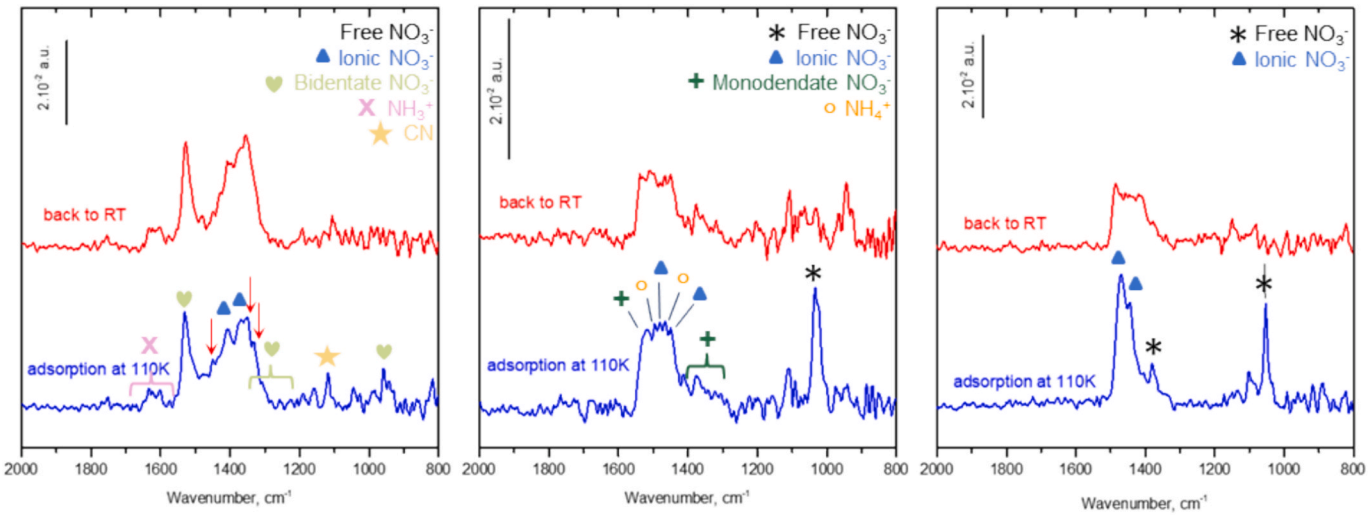

Fig. 7. PM-IRRAS spectra of the $NaNO_3$, NH_4NO_3 and EAN electrosprayed layers recorded at 110 K (in blue) and after 1 h back at RT (in red).

Table 2
Different vibrational modes identified after the electrospray of $NaNO_3$, NH_4NO_3 and EAN at 110 K and at RT.

	Nitrate group vibrations (cm^{-1})		Ammonium group vibrations (cm^{-1})		Alkyl chain group vibration (cm^{-1})	
	This work	Literature	This work	Literature	This work	Literature
$NaNO_3$	Ionic: 1488, 1470 1340 Free: 1380 & 1050	[17–26]	–		–	
NH_4NO_3	Monodentate: 1519 Ionic: 1479 & 1450 Free: 1376	[18,21,28]	$\nu_4(NH_4^+)$ 1494 – 1462 region	[28]	–	
EAN	Bidentate: 1530 1404 & 1367	[18,21]	$\delta(NH_3^+)$ 1633–1577 region	$\delta(NH_3^+)$ –1614 [15,29–32]	$\delta(CH_2)$ 1454ω (CH_2) 1330 ν_a(CCN) 1117	ω(CH_2), δ(CH_2),ω (CH_3) ν_{as}(CCN) [15,30,35,51]

and Auger Cu $L_3M_{45}M_{45}$, and $\lambda^{Cu}_{AugerCu}$ is the elastic mean free path of the Auger electrons of the Cu in the Cu substrate. For both elements, O1s and N1s, two binding energies were used and are reported in Fig. 6. For the oxygen and for the nitrogen atom. The number of oxygen atoms per nm^2 evolves in two stages: a rapid increase during the first ~5 mins of spray time, reaching a value of ~4 oxygen atoms. nm^{-2} for the 530 eV and 532 eV binding energy, followed by a slower growth up during the next 40 mins. Interestingly, the 530 eV contribution plateaus after 5 mins, indicating a saturation of the [**O**-Cu] species at the interface. The nitrogen signal at 400 eV, associated with [C-**N**$H_{x<3}$], follows the same trend, confirming that the species reside at the EAN-Cu interface. Conversely, the signal at 532 eV (O1s) and the 407 eV (N1s), corresponding to nitrate and ammonium group not interacting with the substrate, continue to rise progressively until saturation.

Conversely, the N1s peak at 402 eV binding energy, increases progressively, although it does not follow the same kinetic trend. Additionally, the N/O ratio exceeds the expected 2/3 of the EAN molecule, which can be explained by the partial deprotonation of the ammonium headgroup during the XPS measurement. This experiment reveals the presence of interfacial species until surface saturation ~5 mins and the continuous buildup of EAN molecules at intermediate times (about 20 mins) until complete saturation (from 30 mins to 45 mins).

3.4. d) PM-IRRAS measurement of $NaNO_3$, NH_4NO_3 and EAN at 110 K and after going back to RT

PM-IRRAS analysis was conducted to investigate possible differences in molecules orientation and whether such effect can explain reactivity trends observed by XPS. The spectra acquisition was performed after electrospraying for more than 5 mins (to ensure full surface coverage) at 110 K, then again after returning to room temperature. The results are shown in Fig. 7.

3.4.1. $NaNO_3$ adsorption on Cu (110)

The analysis of the surface after the adsorption of $NaNO_3$ at 110 K reveals the presence of 4 characteristic bands (Table 2). The most intense band is observed at 1470 cm^{-1} with a shoulder at 1440 cm^{-1}, and additional features at 1380 and 1050 cm^{-1}. The spectra of the $NaNO_3$ layer after 1 h reveal the presence of one large band, which might be composed of several bands. The first one at 1488 cm^{-1} is accompanied by a shoulder that extends into the 1380–1340 cm^{-1} region. Interestingly, the intense band previously observed at 1050 cm^{-1}, which was attributed to the ν_1 symmetric stretching mode of free NO_3^- [17–19] is no longer present, suggesting that the interface is mainly composed of NO_3^- species bound with the surface. Several contributions are observed in the 1290–1250 cm^{-1} region. Nitrate anions are known to exhibit several characteristic vibration modes, which are sensitive to their configuration. Nitrate anions exhibit a D_{3h} symmetry [20–22], which results in six vibrational degrees of freedom from which four principal divided in two main categories: two stretching and two bending modes. In the IR region, only the two bending modes and the antisymmetric stretching (ν_3) are active. However, solvents or counterions can disrupt the original D_{3h} symmetry [20,21], activating otherwise forbidden modes and causing splitting, particularly in the ν_3

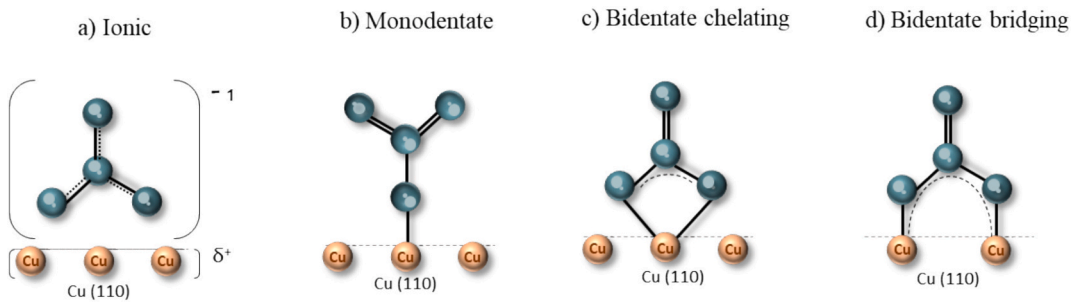

Fig. 8. Schematic configuration of the different nitrate geometries interacting with the Cu (110) and encountered in this work resulting from changes in the cation nature. The ionic form (a) was found in all configurations ($NaNO_3$, NH_4NO_3 and EAN), and the NO_3^- in ionic configuration [26] was primarily seen the $NaNO_3$ molecule. On the other hand, the monodentate form, was seen for the NH_4NO_3 and finally the chelating and/or bridging- corresponding to the most stable configuration were found in EAN explaining the changes in reactivity found previously.

antisymmetric band. In this configuration, the 1380 cm^{-1} band represents the ν_3 asymmetric mode also observed for $NaNO_3$ at 110 K [18]. A second band, which corresponds to the ν_1 symmetric stretching, is observed at 1050 cm^{-1} usually inactive in the IR domain [17,23]. In this case, the presence of positively charged species, such as the Na^+ counterion or Cu surface, can locally alter the electronic structure of NO_3^-, causing a distortion from its original D_{3h} symmetry [22]. Once bound to the surface, the ν_3 splitting occurs, its magnitude depending on the coordination geometry. Significant disagreements can be found in the literature regarding the band attribution of surface nitrates as a function of their structure, but it has been consistently reported that the variations in NO_3^- symmetry (*i.e.,* from D_{3h} to C_{2v}) [17,23] associated to the transformation from ionic NO_3^- to surface-bound NO_3^- [24]: from ionic to monodentate, chelated bidentate, to bridged bidentate nitrates, in correlation with the stability of the species [18,19,21,22,25]. The spectra at 110 K $NaNO_3$ PM-IRRAS mainly reflect ionic NO_3^-, with characteristic features at 1380 cm^{-1} [18] and 1050 cm^{-1}, which were reported to be in this case ionic nitrate [17,26]. The nature of the bonding of these surface nitrates cannot be determined unequivocally; however, the large band at 1470 cm^{-1} as well as the activation of the ν_1 symmetric stretching band at 1050 cm^{-1} [23] clearly imply that part of the nitrate species is no longer in the ionic form.

At RT, the spectrum changes noticeably: the band at 1380 cm^{-1} of free NO_3^- disappears, the intense band initially observed at 1470 cm^{-1} is slightly shifted, and a new, intense band appears at 1488 cm^{-1}. Shoulders corresponding to the vibration band of free nitrates [17,19] at 1380 cm^{-1} and 1340 cm^{-1} remain, suggesting monodentate coordination [19]. A secondary band previously linked to the splitting of ν_3, which appears around 1290–1250 cm^{-1} [18,25]. A weak band at 991 cm^{-1}, possibly ν_1, is detected, whereas another feature which appears at 1152 cm^{-1}, may reflect perturbed symmetric stretches. Importantly, the absence of the second ν_3 splitting band is consistent with the surface selection rules of the PM-IRRAS, which is sensitive only to vibrational modes inducing dipole moment changes perpendicular to the surface [27]. According to Klingenberg and Vannice [26], this component arises from an in-plane bending vibration, which is oriented parallel to the surface and therefore remains undetected in PM-IRRAS spectra.

3.4.2. NH_4NO_3 adsorption on Cu (110)

The 100 K spectrum of NH_4NO_3 reveals a broad band with peaks at 1519, 1494, 1479, 1462, 1450 cm^{-1}, followed by weaker signal at 1376 cm^{-1}, and a shoulder spanning from 1376 to 1300 cm^{-1} (Table 1). A strong band is also observed at 1033 cm^{-1}. In addition to NO_3^-, bands at 1494 and 1462 cm^{-1} are characteristic of $v_4(NH_4^+)$ vibration [28]. The other bands observed have been previously attributed, in the case of $NaNO_3$, to the presence of multiple NO_3^- configurations. The band at 1376 cm^{-1} corresponds to free nitrate, as observed in $NaNO_3$, while the bands at 1479 and 1450 cm^{-1} suggest the presence of ionic nitrate species, stabilized either by NH_4^+ or weak surface physisorption. Most importantly, a distinct band at 1519 cm^{-1} appears, indicating a larger splitting than what was seen previously on the $NaNO_3$ spectra, likely resulting from monodentate coordination, as previously reported [18]. Interestingly, at RT, the spectrum remains similar, except for the absence of the intense band at 1380 cm^{-1} (free NO_3^-), suggesting that all the nitrate species are surface-bound, likely in a monodentate configuration.

3.4.3. EAN adsorption on Cu (110)

The PM-IRRAS spectrum of the EAN at 110 K is markedly different from what was observed for $NaNO_3$ and NH_4NO_3. Multiple sharp and intense bands appear in the 1600 – 1000 cm^{-1} region, suggesting the formation of a well-organized layer on the surface. Three distinct regions can be identified. The first one, at about 1600 cm^{-1}, features several bands of relatively low intensities, which can be attributed to characteristic NH_3^+ vibrational modes [29–32]. Similar observations were reported by Humblot et al. for L-Lysine adsorption on Cu (110)- similar peak at 1614 cm^{-1} ascribed to the δNH_3^+ antisymmetric deformation mode [30]. Peaks at 1633, 1601 and 1577 cm^{-1} suggest overlapping modes due to high surface coverage. The presence of these bands clearly indicates the presence of the NH_3^+ head group of the ethylammonium cation [29–32]. The presence of the alkyl chain is evidenced by bands associated with C–H vibration modes, such as a small shoulder at 1330 cm^{-1} in the second region. In this same region, an intense band at 1530 cm^{-1} is observed, which is a characteristic splitting band associated to surface NO_3^- [21,24]. The magnitude of the splitting, larger than in $NaNO_3$ and NH_4NO_3, is consistent with bidentate configuration [19]. However, the absence of the second band split due to the surface selection rules of PM-IRRAS [27] prevents a clear distinction between bridging or chelating bidentate mode, as illustrated in Fig. 8. A broad region of overlapping peaks between 1454 and 1330 cm^{-1}, reflects the presence of several vibration modes. This region includes bands attributed to NO_3^- species, not bound to the surface, likely adsorbed after full surface coverage (e.g., at 1404 and 1367 cm^{-1}) [26], as well as δCH_2 deformation (1454 cm^{-1}) [33] and ωCH_2 wagging (1330 cm^{-1}) [34] modes. In the third region, between 1200 and 800 cm^{-1}, only one weak contribution at 1117 cm^{-1} corresponds to the CC–N vibration mode [15,35].

At RT, the spectrum shows limited changes, except in the 1500–1300 cm^{-1} region, where bands at 1454 cm^{-1} and 1117 cm^{-1} associated with δCH_2 [33] and the C–N vibration vanish. This agrees with XPS results, indicating partial cleavage of the [C–N] bond due to the reaction between the ethylammonium cation and the Cu substrate upon thermal relaxation to RT. Interestingly the band pattern near 1600 cm^{-1} persists, suggesting that part of the ethylammonium cation remains intact, likely due to high surface coverage. Unambiguously, the PM-IRRAS results confirm that, even at RT, the ionic liquid layer remains partially stable on Cu (110).

4. Discussion

In the context of this work, a previous study by Benbouzid et al. reported substantial changes in the reactivity of NO_3^- towards an Al-Cu-Mg alloy, when introduced in the form of EAN ($CH_3CH_2NH_3NO_3$), compared to a NO_3^- supplied as sodium nitrate ($NaNO_3$). Specifically, these changes were observed during the anodic and cathodic potentiodynamic polarisation test. On the anodic site, Al passivation was shown to result from NO_3^- reduction at the surface, with a one order of magnitude decrease in anodic current density when nitrate was introduced as $CH_3CH_2NH_3NO_3$. Conversely, the cathodic kinetics increased, coinciding with the partial dissolution of the Cu-rich intermetallic particles within the Al-Cu-Mg alloy.

In the present work, XPS results similarly reveal that nitrate anions interact with the Cu atoms, resulting in three different NO_3^- bonding configurations, whether the NO_3^- ions are introduced via $NaNO_3$, NH_4NO_3 or $CH_3CH_2NH_3NO_3$. Following the adsorption of EAN and NH_4NO_3, the XPS spectra show clear evidence of Cu oxidation, accompanied by a significant deprotonation of the ammonium cation. These are in good agreement with previous report on NO_3^- reduction at Cu surfaces in various environments [36–40], including alkaline, acidic, and chloride containing media, as well as in liquid and gas phases as reported by Turnbull et al. and Yoshioka et al.[41,42] as illustrated in Eq. (2):

$$NO_{3(ad)}^- \rightarrow NO_{2(ads)}^- \rightarrow NO_{(ads)} \begin{cases} \nearrow\ NH_4^+ \\ \searrow\ N_2O_{(ads)} \rightarrow N_2 \end{cases}$$
$$NO_{(aq)} \begin{cases} \nearrow \\ \searrow\ NH_4^+ \end{cases} \tag{2}$$

For example, Butcher et al. investigated NO_3^- reduction pathways on Cu single crystal using experimental and modelling techniques such as Raman spectroscopy, SHINERS (Shell-Isolated Nanoparticle-Enhanced Raman Spectroscopy), and DFT calculations [38]. They attributed the observed differences in reactivity on three different Cu crystallographic orientations to variations in the NO_3^- adsorption binding energy and in the oxide (Cu_2O) formation rate. Among the surface studied, Cu (110) exhibited the strongest binding for NO_3^- (−2.80 eV) compared to −2.28 eV and −2.69 eV and Cu (100) respectively. The corresponding reaction pathway, involving the formation of both nitrite species and copper oxide, can be described by the following overall reaction:

$$NO_3^- + 2\,Cu(110) \rightarrow NO_2^- + Cu_2O\,(110) \tag{3}$$

The formation of NO_2^- species has in fact been reported in several studies, spanning from electrocatalysis to corrosion science. For example, Pérez-Gallent et al. observed the formation of nitrites species under alkaline conditions during the reduction of nitrates on Cu single crystal [36]. Interestingly, the nitrate reduction mechanism has also been investigated on Cu-rich intermetallic particles present in Al-Cu-Mg alloys, by Adams et al. proposed a multi-step reaction pathway, describing the sequential conversion of NO_3^- as [43]:

$$NO_3^- + 2e^- + H_2O \rightarrow NO_2^- + 2OH^- \quad E^\circ = 0.01V \tag{4}$$

$$NO_2^- + 6e^- + 5H_2O \rightarrow NH_3 + 7OH^- \quad E^\circ = -0.48V \tag{5}$$

corresponding to the NO_3^- reduction into NO_2^- (4), and followed by NO_2^- reduction into ammonia (5) yielding to the chemical dissolution of Cu rich intermetallic by NH_3 as:

$$Cu + 4NH_3 \rightarrow Cu(NH_3)_4^{2+} \tag{6}$$

Contrastingly, Turnbull et al. [42,44] reported a different multistep oxidation mechanism, in which the oxygen reduction reaction plays a central role. According to their findings, oxygen adsorption and subsequent reduction, lead to the formation of $Cu^+_{(ads)}$ which can act as a catalyst to accelerate oxygen reduction reaction. In the presence of Cu(I) species, NO_3^- reduction can occur, yielding NO_2^- species and concomitant formation of Cu(II). Their key conclusion is that NO_3^- alone does not induce Cu oxidation; rather the presence of both O_2 and NO_3^- species induces copper oxidation.

Despite significant differences in the experimental conditions, these literature results corroborate XPS results of the present work. For $NaNO_3$, the XPS spectra at RT show that the reactivity of NO_3^- alone on Cu (110) is minimal in absence of O_2. In fact, only a small peak at 404 eV is observed in the N 1s region following the electrospray deposition of $NaNO_3$ at RT. In contrast, a strong contribution at 406 eV associated with the formation of $NO_{x<3}$ (e.g., NO_2^-, NO, or N_2O) was clearly identified in the spectra of NH_4NO_3 and EAN. Similar observations have been reported in studies involving ammonia decomposition on Cu single crystal and the catalytic reduction of nitrate on Cu-based nanoparticles, as discussed by Barrabés et al. [40]. These studies showed that the nitrate reduction pathway on Cu may lead to NO_2^-, N_2, or NH_4^+, in agreement with our observations. However, the PM-IRRAS results do not indicate the presence of nitrito or N_2 species at the surface. The absence of these characteristics bands could be explained in two different ways, i) either the nitrito species were poorly organised on the substrate, a configuration unfavourable for PM-IRRAS analysis [27] ii) or, alternatively, these species may have desorbed from the surface prior or during spectral acquisition.

In contrast to previous studies, the differences in reactivity observed in this work are not driven by changes in the substrate composition or crystallographic orientation, but rather by the nature of the counterion. Nevertheless, the exact role of the ammonium and ethylammonium cations remains elusive. The XPS data indicate a deprotonation of the ammonium headgroup and a partial cleavage of the C–N bond. Conversely, the PM-IRRAS experiments do not provide any conclusive evidence regarding possible products formed following the adsorption of EAN at RT. As in the case of nitrito species, this may be due to desorption after formation or poor molecular organisation at the substrate, making them invisible to PM-IRRAS. Undeniably, XPS results reveals that the highest reactivity towards the Cu substrate arises when nitrate is introduced in the form of NH_4NO_3 or $CH_3CH_2NH_3NO_3$, suggesting that presence of an ammonium cation significantly influences the NO_3^- interaction with the metal surface. This hypothesis is supported by the PM-IRRAS results (Fig. 7), which show marked changes in the NO_3^- vibration modes. The magnitude of the splitting bands observed on the 1600–1100 cm^{-1} regions corroborates the changes in binding nature changing from NO_3^- ionic splitting for $NaNO_3$ to monodentate to bidentate chelating configuration in the presence of NH_4^+ and $CH_3CH_2NH_3^+$, respectively as illustrated in Fig. 8. As for the reactivity of the ammonium headgroup itself, several hypotheses can be considered. First, the XPS results show the presence of a $NH_{x<3}$ following the adsorption of both NH_4NO_3 and EAN. In the case of EAN, deprotonation of the ammonium is also accompanied by a partial loss of molecular stoichiometry, reflected by changes in the C–N/C–H ratio. In addition, the intensity of the $NH_{x<3}$ peak is significantly higher for EAN than for NH_4NO_3. Although the synergistic role of $CH_3CH_2NH_3^+$ and NO_3^- remains speculative, a three-stage reaction pathway may explain these observations. As shown by the data, Cu oxidation in the presence of NO_3^- results in the formation of oxidised Cu species at the surface. These surface oxides likely promote progressive deprotonation of the ammonium headgroup (NH_4^+ or $CH_3CH_2NH_3^+$), yielding their conjugated bases (NH_3 and $CH_3CH_2NH_2$, respectively). This would account for the appearance of the $NH_{x<3}$ peak and possibly yield to a partial hydroxylation of the Cu surface. The resulting amines (NH_3 or $CH_3CH_2NH_2$) may readily adsorb or further decompose at the surface, as previously

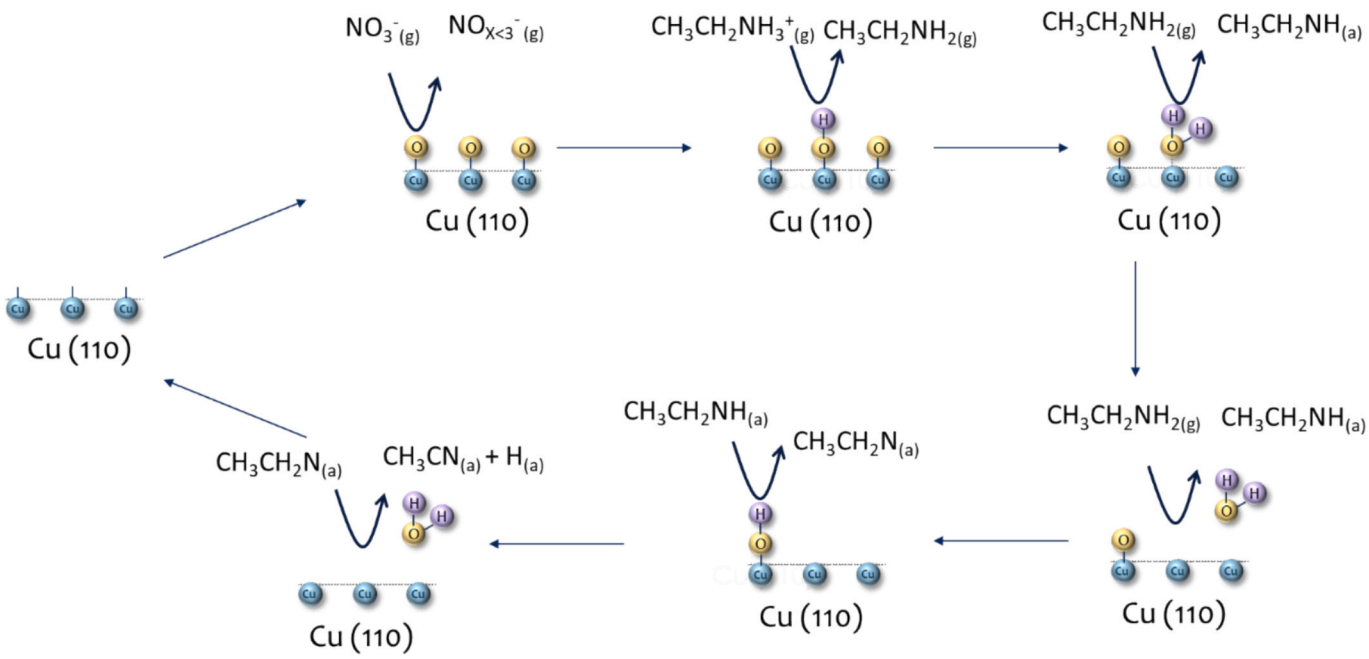

Fig. 9. Schematic figure of the proposed multistep mechanism, involving first the Cu-oxidation from nitrate reduction, followed by the deprotonation and dehydrogenation of the ethylammonium head yielding to a Cu surface hydroxylation. The series of dehydrogenation steps would eventually lead to the formation of water molecules, that would rapidly desorb and expose metallic Cu surface.

shown by [45,46]. They showed by PM-IRRAS that the presence of oxygen was pivotal in the dehydrogenation process, yielding to the progressive formation of NH_2, NH and N_2 species only in the case of pre-oxidised Cu.

Finally, the greater reactivity observed for ethylammonium cations may be explained by the inductive effect of the alkyl group, known to increase the basicity of the amine (*i.e.,* propensity to give electron) and form stable amine-oxygen complexes as reported in previous works [47–49]. In particular, Davies et al. [50] and Thornburg et al. [51,52] studied the reactivity of amines on clean and oxygen pre-covered Cu (110) and Ag (110) surfaces. Their results showed that ethylamine undergoes a cascade of deprotonation/dehydrogenation steps when exposed to the negatively charged interfacial oxygen from the Cu oxide, leading to the formation of amine described in the following reaction sequence:

$$CH_3CH_2NH^+_{3(g)} + O^{2-}_{(ads)} \rightarrow CH_3CH_2NH_{2(a)} + OH^-{}_{(ads)}$$

Followed by the formation of an amide:

$$CH_3CH_2NH_{2(a)} + O_{(a)} \rightarrow CH_3CH_2NH_{(a)} + OH_{(a)}$$

Which dehydrogenate further to an ethyl-imide:

$$CH_3CH_2NH_{(a)} + O_{(a)} \rightarrow CH_3CH_2N_{(a)} + OH_{(a)}$$

These dehydrogenation steps were concomitant with surface hydroxylation, also observed in the present work through the presence of the OH peak on the O1s spectrum and the deprotonated ammonium signal on the N1s spectrum. These processes were subsequently followed by hydroxyl-recombination reactions, leading to the formation of water molecules, which then desorbed from the surface:

$$2OH_{(a)} \rightarrow H_2O_{(g)} + O_{(a)}$$

The nature of the final products was proposed to be acetonitrile (formation and then desorption), which would explain the changes in C–N/C–C peak ratios on the C1s spectrum:

$$CH_3CH_2N_{(a)} \rightarrow CH_3CN_{(g)} + 2H_{(a)}$$

In this context, it explains the increased reactivity of ethylammmonium towards the Cu surface.

5. Conclusion

This investigation provides valuable molecular-level insights into the interfacial reactivity of ionic liquids with reactive metal surfaces. A combined XPS and PM-IRRAS analysis was conducted on electrosprayed $NaNO_3$, NH_4NO_3 and $CH_3CH_2NH_3NO_3$ (EAN) deposited on a Cu (110) single crystal, in order to decipher the individual and combined reactivity of the anion and cation. Initially, each molecule was physisorbed at 110 K, and the results confirmed successful molecular deposition onto the metal via electrospray. Upon returning the system at RT, NO_3^- reduction was observed only for NH_4NO_3 and EAN. Time-resolved electrospray experiments revealed that only the first layer at the interface reacted with the substrate, while subsequent layers remain unreactive, indicating a self-limiting interfacial reaction. In addition, full surface coverage was typically within 5 min of deposition. The PM-IRRAS results showed significant changes in NO_3^- coordination geometry, depending on the nature of the counter-ion. Specifically, NO_3^- adopts an ionic configuration when introduced as $NaNO_3$, shifts to a monodentate configuration when introduced as NH_4NO_3, and form a bidentate coordination in the case of EAN, the latter being previously reported as the most stable binding mode. These observations highlight the critical influence of the cation on both nitrate orientation and surface reactivity. While the results clearly demonstrate the influence of the cationic species, the exact role of the ammonium group, as well as the effect of alkyl chain length in modulating reactivity, remain to be fully elucidated. However, XPS results provide strong evidence of ammonium deprotonation, supporting the formation of the corresponding conjugated bases (NH_3 and $CH_3CH_2NH_2$) for NH_4^+ and CH_3CH_2 NH_3^+, respectively. Based on these observations, a plausible multistep reaction mechanism is proposed as sketched in Fig. 9. It begins with Cu oxidation by NO_3^-, followed by the formation of Cu–O-N coordination complexes between the amine and the copper oxidised surface. The presence of surface oxygen induces successive deprotonation and dehydrogenation steps of the ammonium moiety, generating water molecules that rapidly desorbing, thereby re-exposing metallic Cu, which can in turn be re-

oxidized by NO_3^-. This proposed mechanism can explain the cation – anion synergy responsible for the enhanced reactivity of Cu towards EAN. While the final sequence remains partially speculative and warrants further investigation, the initial sequence is consistent with both XPS and PM-IRRAS results.

In the context of corrosion inhibition applications, these findings provide molecular-level evidence for a synergistic interaction between the cation and anion in ionic liquids. This synergy appears to play a crucial role in modulating surface reactivity, and the insights gained here may have broader applications, not only for corrosion science, but also for more general uses like electrocatalysis and heterogeneous catalysis, where interface stability and design are critical.

CRediT authorship contribution statement

Christophe Méthivier: Writing – review & editing, Visualization, Validation, Methodology, Investigation, Formal analysis, Data curation, Conceptualization. **Mireille Turmine:** Writing – review & editing, Data curation, Conceptualization. **Vincent Vivier:** Writing – review & editing, Validation, Investigation, Conceptualization. **Oumaïma Gharbi:** Writing – review & editing, Writing – original draft, Visualization, Validation, Methodology, Investigation, Formal analysis, Data curation, Conceptualization.

Declaration of competing interest

The authors declare that they have no known competing financial interests or personal relationships that could have appeared to influence the work reported in this paper.

Acknowledgement

The authors would like to thank Pr. Lauron-Pernot for the fruitful discussions.

Appendix A. Supplementary data

Supplementary data to this article can be found online at https://doi.org/10.1016/j.apsusc.2026.166518.

Data availability

Data will be made available on request.

References

[1] F. Endres, Ionic Liquids: Promising Solvents for Electrochemistry, 2004.
[2] C. Verma, E.E. Ebenso, M.A. Quraishi, Ionic liquids as green and sustainable corrosion inhibitors for metals and alloys: an overview, J. Mol. Liq. 233 (2017) 403–414.
[3] A. Chong, J.I. Mardel, D.R. MacFarlane, M. Forsyth, Synergistic corrosion inhibition of mild steel in aqueous chloride solutions by an imidazolinium carboxylate salt, ACS Sustain. Chem. Eng. 4 (2016) 1746–1755.
[4] D. Guzmán-Lucero, O. Olivares-Xometl, R. Martínez-Palou, N.V. Likhanova, M. A. Domínguez-Aguilar, V. Garibay-Febles, Synthesis of selected vinylimidazolium ionic liquids and their effectiveness as corrosion inhibitors for carbon steel in aqueous sulfuric acid, Ind. Eng. Chem. Res. 50 (2011) 7129–7140.
[5] A.Z. Benbouzid, O. Gharbi, N. Sidi-Yakoub, M.T.T. Tran, M. Turmine, V. Vivier, Ionic liquid route for the corrosion inhibition of Al alloys: the effect of butylammonium nitrate on the corrosion of AA2024-T6, Corros. Commun. 9 (2023) 57–64.
[6] J. Sun, P.C. Howlett, D.R. MacFarlane, J. Lin, M. Forsyth, Synthesis and physical property characterisation of phosphonium ionic liquids based on P(O)2(OR)2- and P(O)2(R)2- anions with potential application for corrosion mitigation of magnesium alloys, Electrochim. Acta 54 (2008) 254–260.
[7] P.C. Howlett, S. Gramet, J. Lin, J. Efthimiadis, X.B. Chen, N. Birbilis, M. Forsyth, Conversion coatings of Mg-alloy AZ91D using trihexyl(tetradecyl) phosphonium bis(trifluoromethanesulfonyl)amide ionic liquid, Sci. China Chem. 55 (2012) 1598–1607.
[8] H.H. Elsentriecy, J. Qu, H. Luo, H.M. Meyer, C. Ma, M. Chi, Improving corrosion resistance of AZ31B magnesium alloy via a conversion coating produced by a protic ammonium-phosphate ionic liquid, Thin Solid Films 568 (2014) 44–51.
[9] H.H. Elsentriecy, H. Luo, H.M. Meyer, L.L. Grado, J. Qu, Effects of pretreatment and process temperature of a conversion coating produced by an aprotic ammonium-phosphate ionic liquid on magnesium corrosion protection, Electrochim. Acta 123 (2014) 58–65.
[10] C. Gabler, C. Tomastik, J. Brenner, L. Pisarova, N. Doerr, G. Allmaier, Corrosion properties of ammonium based ionic liquids evaluated by SEM-EDX, XPS and ICP-OES, Green Chem. 13 (2011) 2869–2877.
[11] F. Blin, S. G. Leary, K. Wilson, G. B. Deacon, P. C. Junk, M. Forsyth, Corrosion mitigation of mild steel by new rare earth cinnamate compounds, n.d.
[12] F. Blin, P. Koutsoukos, P. Klepetsianis, M. Forsyth, The corrosion inhibition mechanism of new rare earth cinnamate compounds - Electrochemical studies, Electrochim. Acta 52 (2007) 6212–6220.
[13] H. Gao, N. Xie, H. Wang, M. Chen, J. Zhang, J. Sun, Z. Jin, Evaluation of corrosion inhibition performance of a novel ionic liquid based on synergism between cation and anion, New J. Chem. 44 (2020) 7802–7810.
[14] N. Fairley, V. Fernandez, M. Richard-Plouet, C. Guillot-Deudon, J. Walton, E. Smith, D. Flahaut, M. Greiner, M. Biesinger, S. Tougaard, D. Morgan, J. Baltrusaitis, "Systematic and collaborative approach to problem solving using X-ray photoelectron spectroscopy" Applied Surface Science Advances 2021, 5, DOI 10.1016/j.apsadv.2021.100112.
[15] C. Méthivier, V. Humblot, C.M. Pradier, L-Methionine adsorption on Cu(110), binding and geometry of the amino acid as a function of coverage, Surf. Sci. 632 (2015) 88–92.
[16] E. Rahimi, A. Imani, M. Lekka, F. Andreatta, Y. Gonzalez-Garcia, J.M.C. Mol, E. Asselin, L. Fedrizzi, Morphological and surface potential characterization of protein nanobiofilm formation on magnesium alloy oxide: their role in biodegradation, Langmuir 38 (2022) 10854–10866.
[17] M.H. Brooker, D.E. Irish, G.E. Boyd, Ionic interactions in crystals: Infrared and raman spectra of powdered Ca(NO3)2, Sr(NO3)2, Ba(NO 3)2, and Pb(NO3)2, J. Chem. Phys. 53 (1970) 1228–1234.
[18] M.Y. Mihaylov, V.R. Zdravkova, E.Z. Ivanova, H.A. Aleksandrov, P.S. Petkov, G. N. Vayssilov, K.I. Hadjiivanov, Infrared spectra of surface nitrates: Revision of the current opinions based on the case study of ceria, J. Catal. 394 (2021) 245–258.
[19] K. Hadjiivanov, V. Bushev, M. Kantcheva, D. Klissurski, Infrared spectroscopy study of the species arising during NO2 adsorption on TiO2 (Anatase), Langmuir 10 (1994) 464–471.
[20] D.J. Goebbert, E. Garand, T. Wende, R. Bergmann, G. Meijer, K.R. Asmis, D. M. Neumark, Infrared spectroscopy of the microhydrated nitrate ions NO 3 (H 2O), J. Phys. Chem. A 113 (2009) 7584–7592.
[21] R.E. Hester, W.E.L. Grossman, Vibrational analysis of bidentate nitrate and carbonate complexes, Inorg. Chem. 5 (1966) 1390.
[22] C.C. Addison, N. Logan, S.C. Wallwork, C.D. Garner, Structural aspects of co-ordinated nitrate groups, Q. Rev. Chem. Soc. 25 (1971) 289–322.
[23] P.M. Castro, P.W. Jagodzinski, FTIR and Raman spectra and structure of Cu(NO3)+ in aqueous solution and acetone, Spectrochim. Acta 47A (1991) 1707–1720.
[24] G. Buscaand, V. Lorenzelli, Infrared study of the adsorption of nitrogen dioxide, nitric oxide and nitrous oxide on hematite, J. Catal. 72 (1981) 303–313.
[25] K. Hadjiivanov, H. Knözinger, Species formed after NO adsorption and NO + O2 co-adsorption on TiO2: an FTIR spectroscopic study, PCCP 2 (2000) 2803–2806.
[26] B. Klingenberg, M.A. Vannice, Influence of pretreatment on lanthanum nitrate, carbonate, and oxide powders, Chem. Mater. 8 (1996) 2755–2768.
[27] C. Méthivier, C.-M. Pradier in Characterization of Solid Materials and Heterogeneous Catalysts: From Structure to Surface Reactivity (Eds.: M. Che, J.C. Védrine), Wiley, 2012, pp. 255–287.
[28] H.B. Wu, M.N. Chan, C.K. Chan, FTIR characterization of polymorphic transformation of ammonium nitrate, Aerosol Sci. Tech. 41 (2007) 581–588.
[29] K. Uvdal, P. Bod, A. Ihs, B. Liedberg, W.R. Salaneck, X-ray photoelectron and infrared spectroscopy of glycine adsorbed upon copper, J. Colloid Interface Sci. 140 (1990) 207–216.
[30] V. Humblot, C. Méthivier, C.M. Pradier, Adsorption of L-lysine on Cu(110): a RAIRS study from UHV to the liquid phase, Langmuir 22 (2006) 3089–3096.
[31] S.M. Barlow, K.J. Kitching, S. Haq, N.V. Richardson, A study of glycine adsorption on a Cu{110} surface using reflection absorption infrared spectroscopy, Surf. Sci. 401 (1998) 322–335.
[32] N. Kitadai, T. Yokoyama, S. Nakashima, Temperature dependence of molecular structure of dissolved glycine as revealed by ATR-IR spectroscopy, J. Mol. Struct. 981 (2010) 179–186.
[33] A. Ouasri, A. Rhandour, M.-C. Dhamelincourt, P. Dhamelincourt, A. Mazzah, The infrared and Raman spectra of ethylammonium hexafluorosilicate [C2H5NH3] 2SiF6, Spectrochim. Acta A 59 (2003) 357–362.
[34] Y.C. Farmer, M. Mortland, An infrared study of complexes of ethylamine with ethylammonium and copper ions in montmorillonite, J. Phys. Chem. 69 (1965) 683–686.
[35] M. Diem, Infrared vibration circular dichroism of alanine in the midinfrared region : isotopic effects, J. Am. Chem. Soc. 110 (1988) 6967–6970.
[36] E. Pérez-Gallent, M.C. Figueiredo, I. Katsounaros, M.T.M. Koper, Electrocatalytic reduction of nitrate on copper single crystals in acidic and alkaline solutions, Electrochim. Acta 227 (2017) 77–84.
[37] M. Hou, Y. Tang, J. Xu, Y. Pu, A. Lin, L. Zhang, J. Xiong, X.J. Yang, P. Wan, Nitrate reduction in water by aluminum-iron alloy particles catalyzed by copper, J. Environ. Chem. Eng. 3 (2015) 2401–2407.
[38] D.P. Butcher, A.A. Gewirth, Nitrate reduction pathways on Cu single crystal surfaces: effect of oxide and Cl−, Nano Energy 29 (2016) 457–465.
[39] L. Bai, F. Franco, J. Timoshenko, C. Rettenmaier, F. Scholten, H.S. Jeon, A. Yoon, M. Rüscher, A. Herzog, F.T. Haase, S. Kühl, S.W. Chee, A. Bergmann, R.C. Beatriz, Electrocatalytic nitrate and nitrite reduction toward ammonia using Cu2O

nanocubes: active species and reaction mechanisms, J. Am. Chem. Soc. 146 (2024) 9665–9678.
[40] N. Barrabés, J. Just, A. Dafinov, F. Medina, J.L.G. Fierro, J.E. Sueiras, P. Salagre, Y. Cesteros, Catalytic reduction of nitrate on Pt-Cu and Pd-Cu on active carbon using continuous reactor: the effect of copper nanoparticles, Appl Catal B 62 (2006) 77–85.
[41] T. Yoshioka, K. Iwase, S. Nakanishi, K. Hashimoto, K. Kamiya, Electrocatalytic reduction of nitrate to nitrous oxide by a copper-modified covalent triazine framework, J. Phys. Chem. C 120 (2016) 15729–15734.
[42] J. Turnbull, R. Szukalo, D. Zagidulin, D. Shoesmith, Nitrite effects on copper corrosion in nitric acid solutions, Corros. Sci. 179 (2021), https://doi.org/10.1016/j.corsci.2020.109147.
[43] A.A. Adams, K.E. Eagle, T. Foley, Synergistic effects of anions in the corrosion of aluminum, ECS Electrochem. Lett. 119 (1967) 1692–1694.
[44] J. Turnbull, R. Szukalo, D. Zagidulin, M. Biesinger, D. Shoesmith, The kinetics of copper corrosion in nitric acid, Mater. Corros. 72 (2021) 348–360.
[45] Z. Jiang, P. Qin, T. Fang, Mechanism of ammonia decomposition on clean and oxygen-covered Cu (1 1 1) surface: a DFT study, Chem. Phys. 445 (2014) 59–67.
[46] C.-M. Pradier, A. Adamski, C. Méthivier, I. Louis-Rose, Interaction of NH 3 and oxygen with Cu(110), investigated by FT-IRAS, J. Mol. Catal. A Chem. 186 (2002) 193–201.
[47] H. Umeyama, K. Morokuma, Origin of alkyl substituent effect in the proton affinity of amines, alcohols, and ethers, J. Am. Chem. Soc. 98 (1976).
[48] V.V. Zverev, L.V. Ermolaev, Y.P. Kitaev, A theoretical study of the basicity of methylamines in the gaseous phase, Izvestiya Akademii Nauk SSSR, Seriya Khimicheskaya 26 (1977) 1028–1031.
[49] J.I. Brauman, J.M. Riveros, L.K. Blair, J.I. Brauman, L.K. Blair, J. Amer, Gas-phase basicities of amines, J. Am. Chem. Soc. 16 (1968) 3914–3916.
[50] P.R. Davies, D. Edwards, M. Parsons, Molecularly resolved studies of the role of basicity in the reaction of amines with oxygen at a Cu(1 1 0) surface, Surf. Sci. 601 (2007) 3253–3260.
[51] D.M. Thornburg, R.J. Madix, Cleavage of NH bonds by active oxygen on Ag(ll0) II. Selective oxidation of ethylamine to acetonitrile, Surf. Sci. 226 (1990) 61–76.
[52] D.M. Thornburg, R.J. Madix, Cleavage of N-H bonds by active oxygen on Ag(110) I. Ammonia, Surf. Sci. 220 (1989) 268–294.